

RoDUS: Robust Decomposition of Static and Dynamic Elements in Urban Scenes

Thang-Anh-Quan Nguyen, Luis Roldão, Nathan Piasco,
Moussab Bennehar, and Dzmitry Tsishkou

Noah's Ark, Huawei Paris Research Center, France

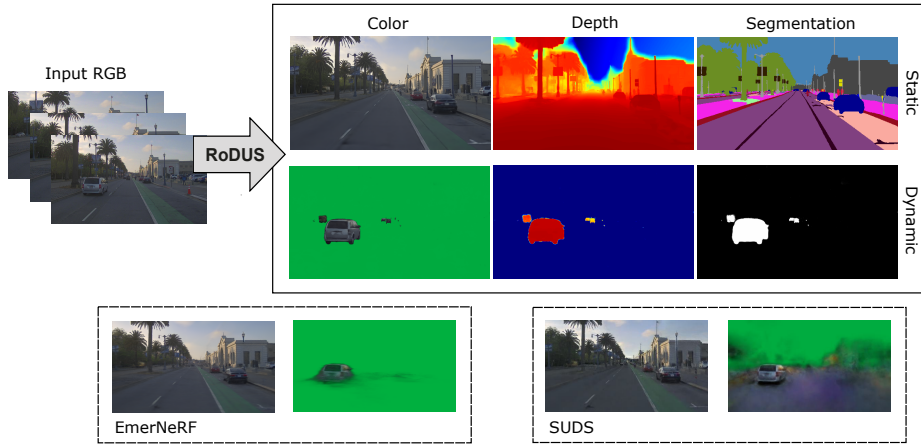


Fig. 1: RoDUS is a neural scene representation designed to decompose 4D dynamic scenes into two elements: moving foreground and static background. This decomposition remains consistent across all photometric, geometric, and semantic aspects.

Abstract. The task of separating dynamic objects from static environments using NeRFs has been widely studied in recent years. However, capturing large-scale scenes still poses a challenge due to their complex geometric structures and unconstrained dynamics. Without the help of 3D motion cues, previous methods often require simplified setups with slow camera motion and only a few/single dynamic actors, leading to sub-optimal solutions in most urban setups. To overcome such limitations, we present RoDUS, a pipeline for decomposing static and dynamic elements in urban scenes, with thoughtfully separated NeRF models for moving and non-moving components. Our approach utilizes a robust kernel-based initialization coupled with 4D semantic information to selectively guide the learning process. This strategy enables accurate capturing of the dynamics in the scene, resulting in reduced artifacts caused by NeRF on background reconstruction, all by using self-supervision. Notably, experimental evaluations on KITTI-360 and Pandaset datasets demonstrate the effectiveness of our method in decomposing challenging urban scenes into precise static and dynamic components.

Keywords: Neural Radiance Fields (NeRFs) · Static-Dynamic Decomposition · Motion Segmentation

1 Introduction

There have been numerous works that achieved success in various 3D representations including both implicit [23] and explicit [36, 37] scene modeling. Therefore, reconstructing and decomposing large-scale dynamic outdoor scenes is becoming a critical task for 3D scene understanding, especially for domains such as closed-loop simulation for autonomous driving [40, 48, 54]. Accurate segmentation and removal of dynamic objects are crucial as they cause floating artifacts during novel view synthesis (NVS) of background scenes due to view inconsistency. This inevitably affects other downstream applications. For instance, several works [7, 12, 20] require masking out eventual dynamic objects as they estimate camera poses. Indeed, in the case of highly dynamic scenes, without feeding the correct masks, they tend to make wrong refinements of the poses. On the other hand, dynamic objects often contain valuable information in the scene and play a main role in tasks such as surveillance and video compression [22].

However, advancements are lagging as understanding time-dependent scenes is still an ill-posed problem. This is because it demands considerable efforts to detect and treat moving components separately, while still ensuring spatio-temporal consistency compared to static scenes [30, 44]. The challenges further arise in driving settings, featuring not only large unbounded scenes, with lots of unconstrained dynamics and various illuminations but also large spatio-temporal gaps captured from the ego-vehicle. This illustrates that a majority of the background regions are captured only for a short duration, due to high occlusion caused by other dynamic objects while the ego-vehicle is also in continuous motion. Unlike previous works [18, 28, 29, 47], where scenes typically involve a single object with slow ego-camera motion, the scenarios encountered in driving sequences are less controllable.

Until now, the research community has proposed various solutions to the challenge of decoupling dynamic objects from static environments. Many of those develop NeRF-based multi-branch architectures in which only the dynamic branch (*i.e.* time-dependent branch) is employed for rendering dynamic objects while the background is learned using a separate static branch. Subsequently, these methods need to detect moving objects offline, so that the static model could later avoid sampling points at regions that belong to dynamic objects [15, 27, 48, 50, 51, 53, 60]. Nevertheless, they end up relying on expensive annotations for segmenting and tracking every object on the scene to enable correct model guidance. Such limitation restricts their adaptability to other datasets. Others [4, 21] learn to classify the inconsistency through a rejection factor while jointly optimizing both branches. However, NeRF’s view-dependent capacity makes it difficult to distinguish non-Lambertian but static from true

dynamic objects, requiring careful and expensive parameter tuning to reach optimal separation.

In this paper, by building upon self-supervised 4D scene representation using NeRF, RoDUS (**R**obust **D**ecomposition of Static and Dynamic Elements in **U**rban **S**cen_es) employs a two-pathway architecture with additional sky and shadow modeling that is suitable for urban scenes. While the architecture is mainly used for representing dynamic scenes as a whole, we argue that there appears the possibility of both branches learning incorrect information (*i.e.* local minima), as long as the overall reconstruction satisfies the ground truth image. This deviates from the initial design intent, where the static branch is meant to learn only the static background, and vice versa. Toward this goal, we inspire from [1] by proposing a robust kernel-based strategy, thus reducing L2 sensitivity. Additionally, we introduce a view-independent semantic field to prevent the static model from expressing unwanted regions, while still being able to refine high-frequency detail. This semantic awareness is further used to guide the information flow, thus balancing the contribution of each branch. To summarize, the main contributions of our work are:

- We demonstrate RoDUS’s capability of static-dynamic decomposition across photometric, geometric, and semantic outputs in a self-supervised manner.
- We introduce a robust initialization scheme and semantic reasoning ability with a masking mechanism that ensures the quality of separation.
- We conduct comprehensive comparisons on several challenging driving sequences, demonstrating our RoDUS’s performance on static-dynamic components extraction, and decoupling compared to other SOTA methods.

2 Related Work

Recently, many works have achieved promising results for high-fidelity view synthesis [2], increasing the training and inference speeds [25], and combining with semantic [9, 13, 15, 58], foundation model-guided [14, 41] reasoning to suit urban driving scenarios [10, 33]. As most of the above methods focus on static scenes, some other works have targeted non-static, transient elements from video sequences [17, 18, 28–30, 44].

NeRFs for outliers rejection. NeRF-W [21] is the pioneering work that decomposes the scene into static and transient components to reconstruct the landmark from unconstrained phototourism datasets. They propose per-frame latent embeddings and a transient head to model different lighting conditions and transient effects, thus these phenomena can be removed from the rendering function at inference. Alternatively, RobustNeRF [34] successfully rejects distractors from the scenes using a trimmed kernel to modify the photometric loss into an Iteratively Least Squares problem, they also propose patch filtering to maintain sharp reconstruction quality. Ha-NeRF [4], instead, parameterizes the kernel as learnable and uses the 2D visibility map per image as a weight function. This occlusion-aware module is proven to be more accurate at separating transient subjects.

Motion segmentation. In addition to advancements in 3D vision, there has been extensive research focusing on self-supervised motion segmentation at 2D image level. The majority of these methods rely on 2D trackers [7], optical flow patterns [3, 16, 55] and/or image warping [35] to distinguish between ego motions and object motions and segment them. These approaches have clear limitations as they focus solely on image-level processing and lack scene-level understanding. Therefore, they struggle to handle complicated static backgrounds with large camera motion [47]. Furthermore, those who follow the pipeline of *first-process-then-NeRF* create not only label ambiguity that affects learning but also add extra costs for separate perception processing tasks, considering that motion segmentation or flow classification themselves are already challenging.

NeRFs for dynamic scene reconstruction. To represent dynamic scenes, a direct solution is to add time as an additional input [17, 32] or learn a deformation field that maps the input coordinates into a canonical space [28, 29]. These time-dependent extensions, however, fail to accurately represent complex scenes and are unable to disentangle the dynamic components. Several works have adopted the idea in multi-branch architectures (*e.g.* NSFF [18], NeuralDiff [42], STaR [56], D2NeRF [47]), decomposing the scene using different radiance fields. Nonetheless, the mentioned methods lack robustness and are not tested in urban driving scenarios where it is much harder to manage the number of dynamic objects within the scene. Consequently, their performance significantly degrades due to the blurriness of dynamic objects and floating artifacts in background regions, restricting their applicability. Follow-up works exploit object-centric approaches, especially NGS [27], PNF [15], and DisCoScene [50] express dynamic scenes and target automotive data, but they are fundamentally constrained by per-scene 3D annotations including bounding boxes and instance tracking which are difficult to obtain reliably without 3D sensors and proper calibration [11].

SUDS [43], and EmerNeRF [52] are the most similar to our approach since they utilize 2D off-the-shelf models to enable object- and scene-level semantic understanding while still being able to separate dynamic objects. Our approach, however, differs from existing works: we pay more attention to the representation of each branch individually, a factor often neglected by other studies but stands advantageous in handling such challenging data. This gives us better performance in lots of downstream tasks such as background reconstruction, object removal, and motion segmentation.

3 Method

This section details RoDUS’s methodology of disentangling and composing representation in addition to its computational pipeline which is illustrated in Fig. 2. We describe in Sec. 3.1 the architecture for our scene representation. In Sec. 3.2, we introduce the semantic-radiance field used in RoDUS, how it can be rendered using differentiable volume rendering and contributes to the separation. Finally, Sec. 3.3 formulates the losses to train RoDUS as well as our proposed training strategy, which is demonstrated in Sec. 3.4.

Goals. Our main goal is to learn a scene representation of a dynamic environment (*e.g.* driving scene) with the ability to semantically disentangle between static components (*e.g.* road, building, vegetation, parked vehicles) and dynamic objects in a self-supervised manner. RoDUS takes a set of N input RGB images of size $W \times H$, their associated poses, and capturing timestamps $\{I_i^{H \times W \times 3}, p_i, t_i\}_{i=1}^N$. Additionally, our model relies on semantic $\{S_i^{H \times W \times L}\}_{i=1}^N$, where L is the number of classes, and geometric cues obtained from pre-trained 2D segmentation model and LiDAR depth measurements, respectively. At inference time, we wish to achieve rendered images for static $\{\hat{I}_i^S, \hat{S}_i^S\}_{i=1}^N$ and dynamic $\{\hat{I}_i^D, \hat{S}_i^D\}_{i=1}^N$ components of the scene for each timestamp independently, which can also be combined for a complete scene. As mentioned above, we study the quality of individual components rather than conforming solely to a satisfying composed result.

3.1 Scene Representation

Preliminaries. RoDUS is based on NeRF [23] which is designed to capture both geometry and view-dependent appearance of a scene from a set of RGB images. It encodes the scene within a Multi-Layer Perceptron (MLP) and outputs color $\mathbf{c}(\mathbf{x}, \mathbf{d}) \in \mathbb{R}^3$ and density $\sigma(\mathbf{x}) \in \mathbb{R}$ at any query position $\mathbf{x} \in \mathbb{R}^3$ along with its viewing direction $\mathbf{d} \in \mathbb{R}^3$. During training, using intrinsic parameters and poses, every pixel of the image undergoes a ray marching procedure \mathbf{r} to sample inputs for the MLP. The model parameters are optimized to predict the colors rendered along the ray using the mean squared error: $\mathcal{L} = \|\hat{\mathbf{C}}_i(\mathbf{r}) - \mathbf{C}_i(\mathbf{r})\|_2^2$.

Architecture. Inspired by [18, 21, 47], we factorize the scene into two elements, each learned through a separate pathway: one for moving components and the other for non-moving background. Each branch is modeled independently using its own multi-level hash grid representation and MLPs. This approach enables the concurrent learning of both static and dynamic aspects of the scene.

The static branch whose mission is to learn all non-moving parts in the scene, uses a 3D hash grid \mathcal{H}^S , analogous to the one used in [25]. To model lighting variations, we also condition on a per-frame latent embedding l_a [21]:

$$(\sigma^S, \mathbf{c}^S, \mathbf{s}^S) = \mathcal{F}_\Theta^S(\mathcal{H}^S(\mathbf{x}), \gamma(\mathbf{d}), l_a). \quad (1)$$

As the dynamic branch allows its outputs to depend on time, we employ a 4D hash grid \mathcal{H}^D with one additional normalized timestamp t as input. The dynamic field additionally incorporates a shadow head [47] designed to learn a shadow ratio $\rho \in [0, 1]$. This scalar is later used to scale down the static radiance values \mathbf{c}^S in Eq. (3):

$$\begin{aligned} (\sigma^D, \mathbf{c}^D, \mathbf{s}^D) &= \mathcal{F}_\Theta^D(\mathcal{H}^D(\mathbf{x}, t), \gamma(\mathbf{d})), \\ \rho &= \mathcal{F}_\Theta^\rho(\mathcal{H}^D(\mathbf{x}, t)). \end{aligned} \quad (2)$$

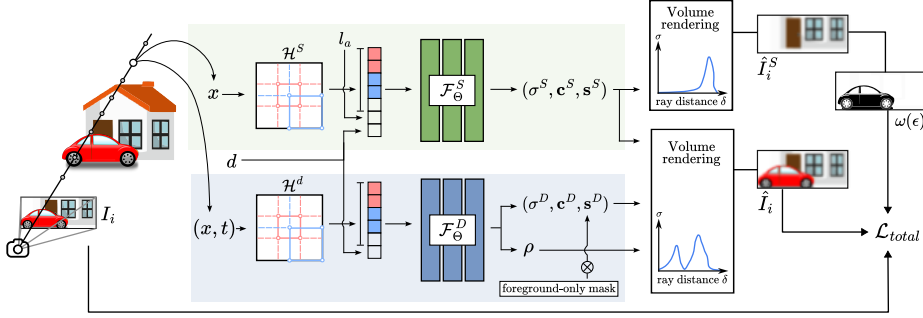


Fig. 2: RoDUS’s architecture. Our model comprises two separate branches that take as input sampled positions \mathbf{x} , their viewing direction \mathbf{d} , and their timestamp t for the dynamic branch, and generate outputs for every query coordinate. Each branch is represented by a separate hash grid and the MLP-based neural function, which predicts colors, densities, and semantics. The rendered static image is used to calculate IRLS map $\omega(\epsilon)$ during the robust initialization step (Sec. 3.3), while dynamic semantic outputs are passed through a “foreground-only mask” to prevent over-explaining background regions (Sec. 3.2).

Rendering. We calculate the color \hat{C} for each camera ray \mathbf{r} by integrating all the sampled points along the ray:

$$\hat{C}(\mathbf{r}) = \sum_{i=1}^K T_i (\alpha_i^S (1 - \rho_i) \mathbf{c}_i^S + \alpha_i^D \mathbf{c}_i^D), \quad (3)$$

where $T_i = \exp\left(-\sum_{j=1}^{i-1} (\sigma_j^S + \sigma_j^D) \delta_j\right)$ is the accumulated transmittance and $\alpha_i^\xi = 1 - \exp(-\sigma_i^\xi \delta_i)$ with $\xi \in \{S, D\}$ are alpha values. Given the outputs of each branch, we can render static and dynamic maps separately.

3.2 Enabling Semantic Awareness

NeRF provides low-level implicit representations of geometry and radiance but lacks a higher-level understanding of the scene. It is shown in [34] that relying only on view-dependent radiance and sensitive mean square error makes the model prone to outliers and over-fit observations. On the other hand, semantic labels can be conceptualized as a *view-invariant* function [59], mapping world coordinates \mathbf{x} to a distribution over semantic labels $\mathbf{s}(\mathbf{x}) \in \mathbb{R}^L$. As a result, we choose to integrate a semantic head to predict the semantic class for each point, similar to the color head. Subsequently, the same rendering formula is applied for semantics to achieve 2D semantic segmentation maps:

$$\hat{S}(\mathbf{r}) = \sum_{i=1}^K T_i (\alpha_i^S \mathbf{s}_i^S + \alpha_i^D \mathbf{s}_i^D). \quad (4)$$

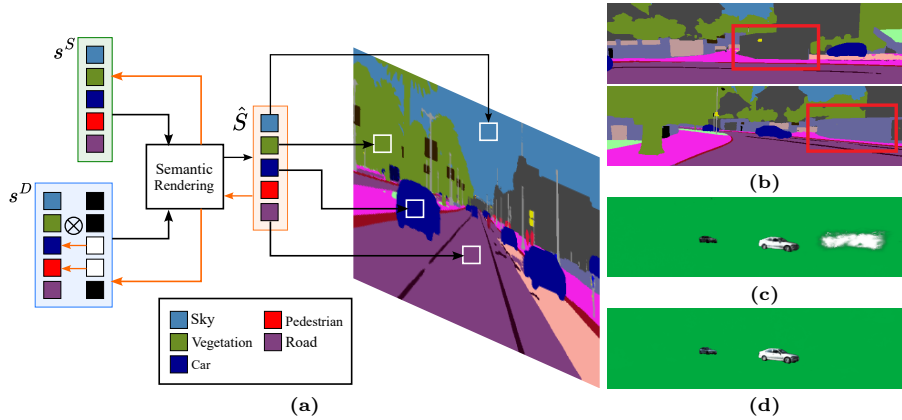


Fig. 3: (a) We enforce a “foreground-only mask” to the dynamic semantic head. In the forward pass (black arrows), the mask prevents the dynamic branch from outputting pixels that do not belong to foreground classes. Similarly, in the backward pass (orange arrows), it restricts the dynamic field from learning background pixels, which may primarily come from noisy annotations. (b) Predictions generated by 2D segmentation model are noisy and inconsistent between views. (c) Since the dynamic field includes a temporal dimension, it ends up learning these conflicting labels, satisfying the overall loss. (d) Therefore, our proposed mask is used to tackle the problem.

The use of semantic supervision in RoDUS serves two main purposes. First, it provides assumptions for multiple classes, forming the basis for the loss formulations (refer to Sec. 3.3) that contribute to enhancing rendering quality. Second, it enables the model to capture detailed scene layout and object boundary information with a high level of precision thereby assisting in decomposition.

One point to consider is that supervision for segmentation with noisy pseudo labels should not impact the underlying geometry. Otherwise, the model can still satisfy conflicting labels by changing the dynamic weights, resulting in the wrong geometry. Previous works [9, 39] stop gradients from the semantic head back to the densities to solve this problem. However, we believe that semantic information plays an important role in correcting the separation. We instead limit the dynamic model from contributing static class prediction to the final results by putting a mask in the last layer of its semantic head. This masking strategy can be viewed as a form of gradient stopping the learning but in a selective way as illustrated in Fig. 3. Note that we do not have motion information for each instance, we only leverage the fact that certain classes are potentially movable to penalize the dynamic model from predicting background (non-movable) samples.

We apply `softmax` normalization at each query point individually before ray integration, as introduced in [39]. This is done due to the unbounded nature of logits, ensuring that the semantic head can not generate excessively high scores in regions with low density to overcome high-density areas. Remarkably, this not only improves the stability of rendering semantics but also prevents half-

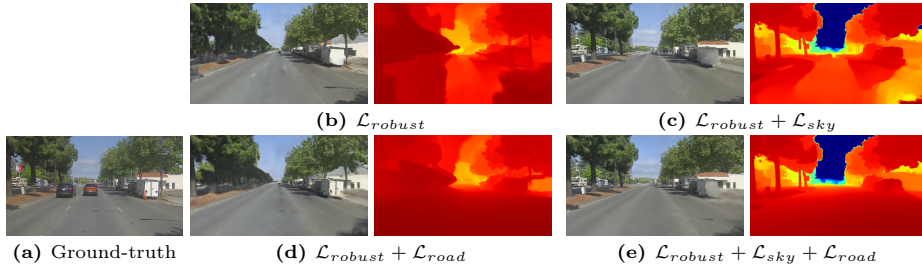


Fig. 4: (b) The use of a trimmed kernel helps completely remove moving cars in the scene. (c, d, e) As the sky and road regions are badly reconstructed, applying class constraints can aid the learning process of the static field.

precision floating point (`float16`) overflowing when working with frameworks such as `tiny-cuda-nn` [24].

3.3 Loss Formulation

Reconstruction losses. Consistent with other NeRF works, we incorporate both L2 and DSSIM [46] losses to supervise the pixel color \mathcal{L}_{rgb} . In cases where LiDAR data is available, depth supervision [8, 33] loss $\mathcal{L}_d = \|\hat{d}_i(\mathbf{r}) - d_i(\mathbf{r})\|_2^2$ is considered to enhance the reconstruction accuracy. In addition, cross-entropy [59] loss is applied to provide supervision on the generated semantic labels derived from pseudo-ground truth segmentation, expressed as $\mathcal{L}_{sem} = CE(\hat{S}(\mathbf{r}), S(\mathbf{r}))$.

Robust loss. Our objective is to reduce the sensitivity of the static model to dynamic objects by incorporating supervision through a robust photometric loss. This loss can be formulated as an Iteratively Reweighted Least Squares (IRLS) problem:

$$\mathcal{L}_{robust} = \kappa \left(\|\hat{C}^S(\mathbf{r}) - C(\mathbf{r})\|_2 \right) = \omega(\epsilon(\mathbf{r})) \cdot \|\hat{C}^S(\mathbf{r}) - C(\mathbf{r})\|_2^2, \quad (5)$$

where $\epsilon(\mathbf{r}) = \|\hat{C}^S(\mathbf{r}) - C(\mathbf{r})\|_2$ is the error residuals and $\omega(\epsilon) = \epsilon^{-1} \cdot \partial\kappa(\epsilon)/\partial\epsilon$ is the weight function of the residuals at the previous iteration. Among the family of kernels [1], we follow Sabour *et al.* [34] and choose a trimmed estimator [6] which classifies outliers based on a percentile threshold \mathcal{T}_ϵ calculated from the whole batch of rays. This choice ensures outliers are completely removed (*i.e.* hard weights). Furthermore, as every object has neighbor connections, they apply a spatial filter \mathcal{F} on the residuals map to capture the smoothness, ensuring local support of the kernel:

$$\omega(\epsilon(\mathbf{r})) = \mathcal{F}[\epsilon(\mathbf{r}) \leq \mathcal{T}_\epsilon], \quad (6)$$

where \mathcal{F} consists of a box filter to diffuse inlier/outlier labels and a sub-patch level consistency filter that takes into account the rejection behavior of its surrounding neighborhoods. This filter aims to remove high-frequency details from being classified as outliers and allows them to be captured by the NeRF models.

Sky loss. Outdoor scenes contain sky regions where rays never intersect any opaque surfaces. We detect pixels that belong to the sky and force the densities to be zeros along the ray, excluding the last sample:

$$\mathcal{L}_{sky} = \mathbb{E} \left[\frac{1}{K-1} \sum_{i=1}^{K-1} \sigma_i + \frac{1}{\sigma_K} \right]_{\mathbf{r} \in \mathcal{R}_{sky}}. \quad (7)$$

Planar regularization loss. We observe that the road surface is challenging to model as it has low textures and is often occluded by moving vehicles. These areas mostly suffer from poor geometry prediction (Fig. 4). To address this issue, we rely on the work of Wang *et al.* [45], perform Singular Values Decomposition (SVD) on the set of centered points projected from patches that are assigned with the road label, and minimize the smallest singular value σ_3 :

$$\mathcal{L}_{road} = \sigma_3(\mathcal{R}_{road}^{patch}). \quad (8)$$

Dynamic regularization loss. We use the factorization $\mathcal{L}_{\mathcal{H}}$ and sparsity $\mathcal{L}_{\sigma^D}, \mathcal{L}_{\rho}$ losses that have been proposed in [38, 47, 56] to enforce the static branch to explain most of the static structure as possible and only express the moving objects and/or shadows using the dynamic branch.

Our final loss results on the weighted sum of all our individual losses:

$$\begin{aligned} \mathcal{L}_{total} = & \underbrace{\mathcal{L}_{rgb} + \lambda_d \mathcal{L}_d + \lambda_{sem} \mathcal{L}_{sem}}_{reconstruction} \\ & + \underbrace{\mathcal{L}_{robust} + \lambda_{sky} \mathcal{L}_{sky} + \lambda_{road} \mathcal{L}_{road}}_{static\ regularization} + \underbrace{\lambda_{\sigma^D} \mathcal{L}_{\sigma^D} + \lambda_{\rho} \mathcal{L}_{\rho} + \lambda_{\mathcal{H}} \mathcal{L}_{\mathcal{H}}}_{dynamic\ regularization} \end{aligned} \quad (9)$$

3.4 Training strategy

The use of robust estimation plays an important role in rejecting inconsistency (dynamic objects in our case) and guiding the static branch without any prior knowledge. However, we observe that using a binary kernel alone with a fixed threshold, after reaching a certain point throughout the training, the robust loss does not contribute to the overall loss anymore. We refer to this phenomenon as “kernel saturation”, this causes several parts of the scene not to be learned completely. Adjusting the threshold \mathcal{T}_{ϵ} seems to be a trivial solution, but given the fact that outdoor scenes are more complicated to handle, there is always a trade-off between the number of distractors removed and the static scene quality. Particularly, high-frequency but static details, equivalently appear as large residuals are considered as outliers, while low-frequency but moving regions such as shadows (**dark**) which mostly share a similar color with the road (**gray**) are uncontrollably included as inliers. Figure 4 portrays this, as there are still parts of the scene (*e.g.* the truck on the right) that are not fully learned by the model.

In contrast, relying solely on reconstruction losses leads to several local optima during optimization due to the entanglement of geometry and appearance.

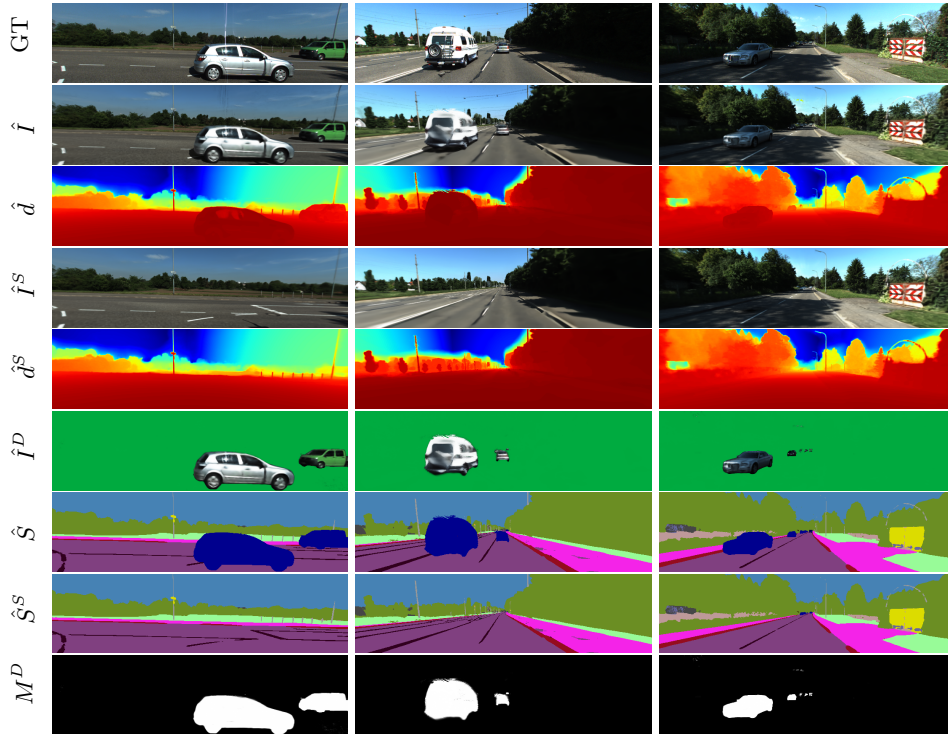


Fig. 5: We demonstrate RoDUS’s capabilities on multiple tasks. Notice that we successfully retain separation consistencies between all photometric, geometric, and semantic outputs. *Legend:* GT: Ground truth, \hat{I} : Composed RGB, \hat{d} : Composed depth, I^S : Static RGB, \hat{d}^S : Static depth, \hat{I}^D : Dynamic RGB (blended with a green background), \hat{S} : Composed segmentation map, \hat{S}^S : Static segmentation map, M^D : Motion segmentation.

We propose using the robust loss as an initialization step for the static model to learn the basic overall structures of the scene before delving into complete scene understanding. The initialization step guides the network to prioritize consistent (or confident) regions that further help stabilize the training process. Therefore, we start the model training with the robust loss (Eq. (5)) and sky loss (Eq. (7)) enabled for the first epoch, and subsequently enable the remaining losses. This serves as a foundation for disentangling the scene in later training stages.

4 Evaluation

4.1 Experimental Setup

Implementation details. We build RoDUS using PyTorch [31]. Our implementation is based on `tiny-cuda-nn` [24] from iNGP [25], and proposal sampling strategy inspired from MipNeRF360 [2]. To generate pseudo-ground truth for

Table 1: Quantitative comparisons with SoTA methods on KITTI-360 and Pandaset.

		Image Reconstruction			Static NVS			Motion segmentation		
		PSNR \uparrow	SSIM \uparrow	LPIPS \downarrow	PSNR \uparrow	SSIM \uparrow	LPIPS \downarrow	Recall \uparrow	IoU \uparrow	F1 \uparrow
KITTI-360	RobustNeRF [34] [†]	-	-	-	19.50	0.722	0.282	-	-	-
	D ² NeRF [47]	23.86	0.688	0.232	18.70	0.588	0.309	12.04	4.67	7.41
	SUDS [43]	28.16	<u>0.836</u>	<u>0.175</u>	18.81	0.687	0.298	93.89	5.35	9.34
	EmerNeRF [52]	25.49	0.798	0.181	<u>20.59</u>	<u>0.733</u>	<u>0.249</u>	57.74	<u>12.56</u>	<u>19.92</u>
	RoDUS (ours)	<u>26.47</u>	0.857	0.148	23.43	0.802	0.181	<u>79.45</u>	64.84	76.52
Pandaset	RobustNeRF [34] [†]	-	-	-	23.41	0.764	0.197	-	-	-
	D ² NeRF [47]	25.25	0.692	0.291	23.38	0.682	0.292	-	-	-
	SUDS [43]	30.28	<u>0.851</u>	<u>0.138</u>	25.34	0.788	0.182	-	-	-
	EmerNeRF [52]	<u>29.51</u>	0.841	0.155	27.47	<u>0.811</u>	<u>0.166</u>	-	-	-
	RoDUS (ours)	28.39	0.877	0.135	<u>25.83</u>	0.825	0.156	-	-	-

[†] As RobustNeRF rejects distractors during training, full image reconstruction metrics are not included.

semantic segmentation, we use the Mask2Former [5] model pre-trained on the Mapillary Vistas [26] dataset.

Datasets. We evaluate our system on two challenging urban driving datasets, KITTI-360 [19] and Pandaset [49], both featuring dynamic objects in driving scenarios. In Pandaset, we utilize three front cameras and one back camera, while in KITTI-360, we use all two perspective cameras along with side fish-eye cameras. For evaluation, we rely on provided ground-truth instance masks (KITTI-360)/projected 3D bounding boxes (Pandaset) with motion labels to identify true dynamic objects. We refer to the supplementary for additional details on the selection of the training sequences and data pre-processing.

Baseline. We benchmark RoDUS against 4 different state-of-the-art methods for static scene extraction (RobustNeRF [34]) and dynamic scene rendering (D²NeRF [47], SUDS [43], and EmerNeRF [52]). Evaluations focus on two key factors: the quality of novel view synthesis of the static image and the segmentation masks of dynamic objects. While our primary focus is on static-dynamic disentanglement, RoDUS’s design allows it to represent dynamic scenes holistically so the quality of the overall image is also considered. In Fig. 5, we showcase the performance of our method on 3 representative challenging scenarios.

4.2 Static-Dynamic Decomposition

We report PSNR, SSIM [46], and LPIPS [57] for both image reconstruction and static NVS tasks. We create a validation set by splitting every 8th image (sorted by timestamps) per camera. In the image reconstruction task, we utilize all available samples of the training set for evaluation. In the static NVS task, we compare the image rendered from the static branch to the ground truth with all true dynamic objects masked out. As illustrated in Fig. 6 and Tab. 1, other methods achieve good rendering quality in the composed image. However, only EmerNeRF and RoDUS achieve reasonable results when rendering each component separately. We also lead in SSIM and LPIPS.

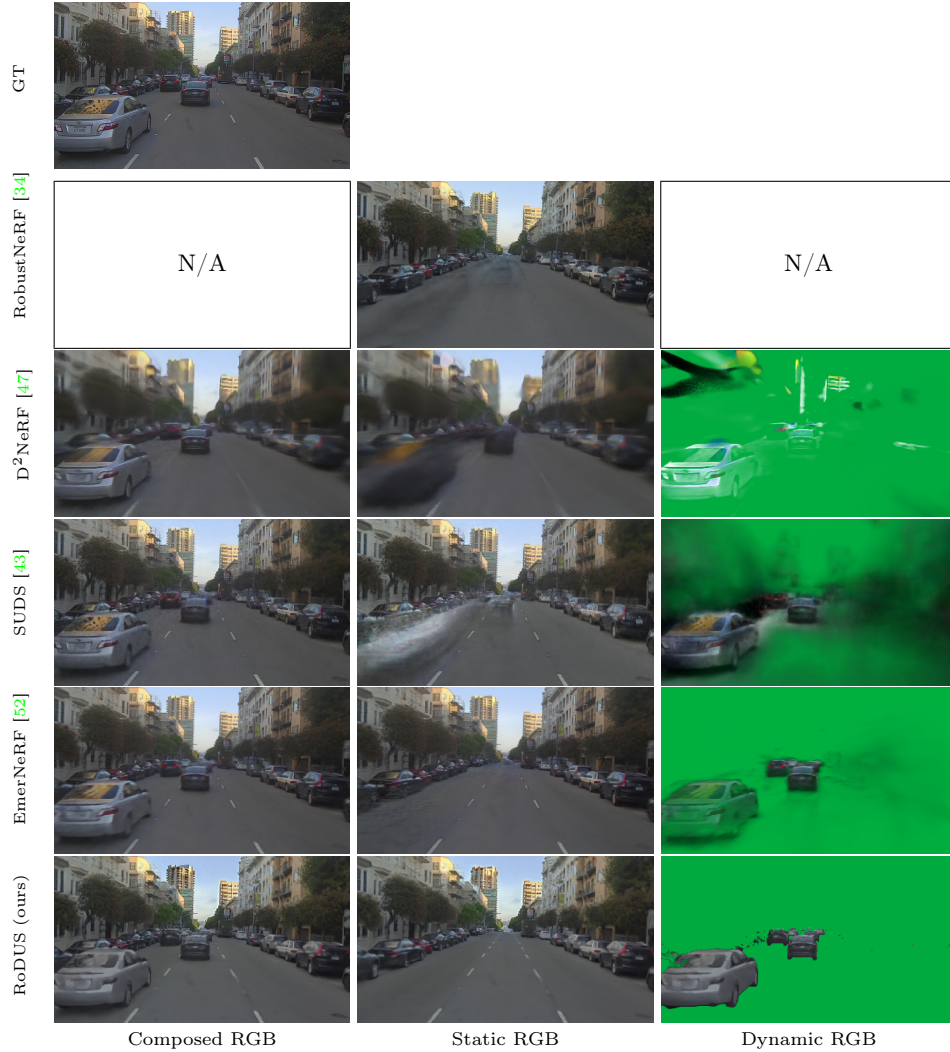


Fig. 6: Reconstruction and decomposition qualitative results comparisons on Pandaset. D²NeRF struggles in intricate driving contexts and produces poor results. SUDS faces difficulties in distinguishing between ego-motion and object-motion due to its reliance on optical flow supervision, leading to a large number of cloudy artifacts in the dynamic image to match the ground-truth optical flows. We can see that the separation between static and dynamic components is still suboptimal. RobustNeRF successfully reconstructs the background with no dynamic objects remaining, but it suffers from saturation, leading to degraded results (as explained in Sec. 3.3). In contrast, RoDUS successfully decouples dynamic objects and achieves a clean background with no artifacts remaining.

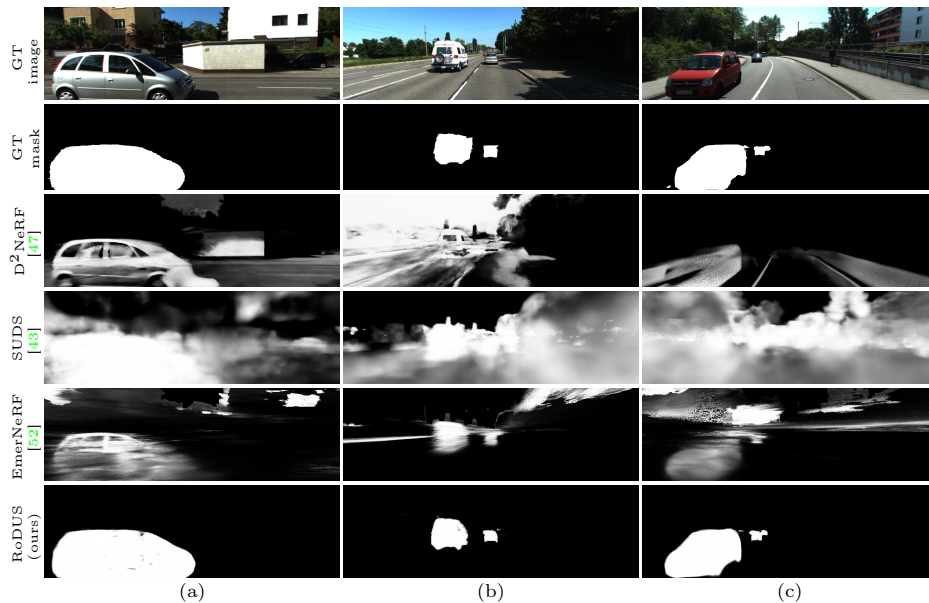


Fig. 7: Motion segmentation qualitative results comparison on KITTI-360 before thresholding. We present results in three scenarios: (a) The ego-car stops in front of an intersection; (b) Vehicles move in the same direction as the ego-car; and (c) Vehicles move in the opposite direction toward the ego-car.

4.3 Dynamic Objects Segmentation

For this task, we obtain the motion mask M^D by rendering dynamic opacity masks and applying a threshold $\mathcal{T}_{OD} = 0.5$. We report mask Recall, IoU, and F1-score on training views. We only evaluate on KITTI-360 due to the absence of ground-truth instance masks in Pandaset. In Fig. 7, we explore various scenarios to understand how the ego-actor moves in relation to other moving objects and how it observes the scenes that could impact the decomposition. Particularly, case (a) is likely the easiest as the background is broadly observed for a long period, we can still notice the mask of moving cars in D²NeRF, SUDS’s results. In cases (b) and (c), when the ego actor is in motion, most methods suffer from incorrect segmentation, while our semantic guidance forces the model to learn the correct dynamic objects. SUDS tends to produce large dynamic areas, resulting in very high Recall but low IoU and F1 while EmerNeRF exhibits sensitivity to lighting variations. Correspondingly, RoDUS’s metrics outperform the others in both key factors in Tab. 1

4.4 Ablation Study

We analyze our design choices in Tab. 2. The use of road, sky regularization, and robust initialization terms support the geometry, especially in regions occluded

by dynamic objects, thus improving the overall quality. Please refer to Fig. 4 and Fig. 8 for visual comparisons.

Table 2: Ablation study. Impact of our design choice on static NVS task.

Ablation	PSNR \uparrow	SSIM \uparrow	LPIPS \downarrow
Full model	25.94	0.814	0.170
w/o \mathcal{L}_d	-0.80	-0.032	+0.023
w/o \mathcal{L}_{sem}	-1.67	-0.080	+0.078
w/o \mathcal{L}_{robust}	-0.91	-0.047	+0.067
w/o \mathcal{L}_{road}	-0.84	-0.035	+0.026
w/o $\mathcal{L}_{\sigma D}$	-0.74	-0.030	+0.024
w/o FG mask	-0.67	-0.035	+0.023

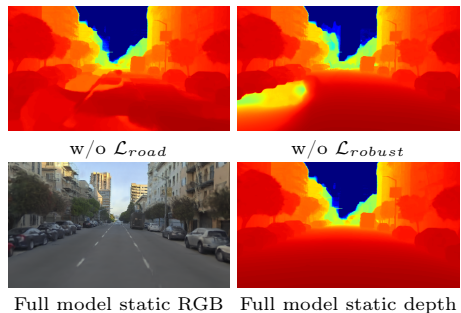


Fig. 8: Static depth map ablation

4.5 Limitation

Our approach can’t handle areas that lack observations or have been highly occluded most of the time within the sequence. This is particularly notable by large or slow-moving objects, illustrated in Fig. 9. Exploring a model that is capable of detecting and inpainting these missing regions based on prior knowledge will be interesting as a future research direction.

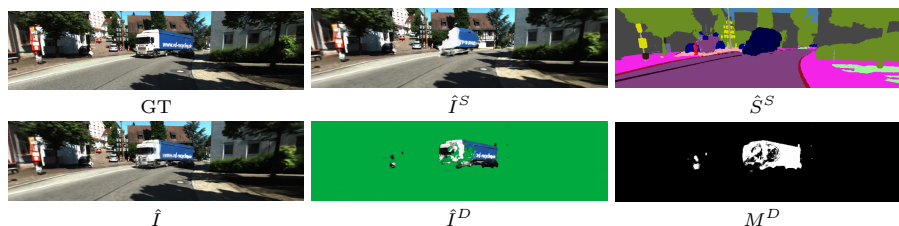


Fig. 9: Failure case. The static field is unable to recover regions that are highly occluded by the truck due to its lack of generalizing ability to unseen backgrounds. On the other hand, the dynamic field doesn’t support object-level connection, leading to only half of the truck being visible in dynamic outputs.

5 Conclusion

In this paper, we presented RoDUS, a method for disentangling dynamic scenes using neural representation. Our approach effectively separates moving components from the scene without the need for manual labeling. To enhance disentangling efficiency, we proposed a robust training strategy and incorporated semantic reasoning, resulting in high-quality background view synthesis and accurate segmentation. We conducted extensive experiments on challenging autonomous driving datasets, showcasing that RoDUS surpasses current state-of-the-art NeRF frameworks.

References

1. Barron, J.T.: A general and adaptive robust loss function. In: Proceedings of the IEEE/CVF Conference on Computer Vision and Pattern Recognition. pp. 4331–4339 (2019) [3](#), [8](#)
2. Barron, J.T., Mildenhall, B., Verbin, D., Srinivasan, P.P., Hedman, P.: Mip-nerf 360: Unbounded anti-aliased neural radiance fields. In: Proceedings of the IEEE/CVF Conference on Computer Vision and Pattern Recognition. pp. 5470–5479 (2022) [3](#), [10](#), [19](#)
3. Cao, Z., Kar, A., Hane, C., Malik, J.: Learning independent object motion from unlabelled stereoscopic videos. In: Proceedings of the IEEE/CVF Conference on Computer Vision and Pattern Recognition. pp. 5594–5603 (2019) [4](#)
4. Chen, X., Zhang, Q., Li, X., Chen, Y., Feng, Y., Wang, X., Wang, J.: Hallucinated neural radiance fields in the wild. In: Proceedings of the IEEE/CVF Conference on Computer Vision and Pattern Recognition. pp. 12943–12952 (2022) [2](#), [3](#)
5. Cheng, B., Misra, I., Schwing, A.G., Kirillov, A., Girdhar, R.: Masked-attention mask transformer for universal image segmentation. In: Proceedings of the IEEE/CVF conference on computer vision and pattern recognition. pp. 1290–1299 (2022) [11](#)
6. Chetverikov, D., Svirko, D., Stepanov, D., Krsek, P.: The trimmed iterative closest point algorithm. In: 2002 International Conference on Pattern Recognition. vol. 3, pp. 545–548. IEEE (2002) [8](#)
7. Deka, M.S., Sang, L., Cremers, D.: Erasing the ephemeral: Joint camera refinement and transient object removal for street view synthesis. arXiv preprint arXiv:2311.17634 (2023) [2](#), [4](#)
8. Deng, K., Liu, A., Zhu, J.Y., Ramanan, D.: Depth-supervised nerf: Fewer views and faster training for free. In: Proceedings of the IEEE/CVF Conference on Computer Vision and Pattern Recognition. pp. 12882–12891 (2022) [8](#)
9. Fu, X., Zhang, S., Chen, T., Lu, Y., Zhu, L., Zhou, X., Geiger, A., Liao, Y.: Panoptic nerf: 3d-to-2d label transfer for panoptic urban scene segmentation. In: 2022 International Conference on 3D Vision (3DV). pp. 1–11. IEEE (2022) [3](#), [7](#)
10. Guo, J., Deng, N., Li, X., Bai, Y., Shi, B., Wang, C., Ding, C., Wang, D., Li, Y.: Streetsurf: Extending multi-view implicit surface reconstruction to street views. arXiv preprint arXiv:2306.04988 (2023) [3](#)
11. Herau, Q., Piasco, N., Bennehar, M., Roldão, L., Tsishkou, D., Migniot, C., Vasseur, P., Demonceaux, C.: Moisst: Multi-modal optimization of implicit scene for spatiotemporal calibration. In: International Conference on Intelligent Robots and Systems (IROS) (2023) [4](#)
12. Herau, Q., Piasco, N., Bennehar, M., Roldão, L., Tsishkou, D., Migniot, C., Vasseur, P., Demonceaux, C.: Soac: Spatio-temporal overlap-aware multi-sensor calibration using neural radiance fields. arXiv preprint arXiv:2311.15803 (2023) [2](#)
13. Irshad, M.Z., Zakharov, S., Liu, K., Guizilini, V., Kollar, T., Gaidon, A., Kira, Z., Ambrus, R.: Neo 360: Neural fields for sparse view synthesis of outdoor scenes. In: Proceedings of the IEEE/CVF International Conference on Computer Vision. pp. 9187–9198 (2023) [3](#)
14. Kobayashi, S., Matsumoto, E., Sitzmann, V.: Decomposing nerf for editing via feature field distillation. *Advances in Neural Information Processing Systems* **35**, 23311–23330 (2022) [3](#)
15. Kundu, A., Genova, K., Yin, X., Fathi, A., Pantofaru, C., Guibas, L.J., Tagliasacchi, A., Dellaert, F., Funkhouser, T.: Panoptic neural fields: A semantic object-

- aware neural scene representation. In: Proceedings of the IEEE/CVF Conference on Computer Vision and Pattern Recognition. pp. 12871–12881 (2022) [2](#), [3](#), [4](#)
16. Li, H., Gordon, A., Zhao, H., Casser, V., Angelova, A.: Unsupervised monocular depth learning in dynamic scenes. In: Conference on Robot Learning. pp. 1908–1917. PMLR (2021) [4](#)
 17. Li, T., Slavcheva, M., Zollhoefer, M., Green, S., Lassner, C., Kim, C., Schmidt, T., Lovegrove, S., Goesele, M., Newcombe, R., et al.: Neural 3d video synthesis from multi-view video. In: Proceedings of the IEEE/CVF Conference on Computer Vision and Pattern Recognition. pp. 5521–5531 (2022) [3](#), [4](#)
 18. Li, Z., Niklaus, S., Snavely, N., Wang, O.: Neural scene flow fields for space-time view synthesis of dynamic scenes. In: Proceedings of the IEEE/CVF Conference on Computer Vision and Pattern Recognition. pp. 6498–6508 (2021) [2](#), [3](#), [4](#), [5](#)
 19. Liao, Y., Xie, J., Geiger, A.: Kitti-360: A novel dataset and benchmarks for urban scene understanding in 2d and 3d. *IEEE Transactions on Pattern Analysis and Machine Intelligence* **45**(3), 3292–3310 (2022) [11](#)
 20. Liu, Y.L., Gao, C., Meuleman, A., Tseng, H.Y., Saraf, A., Kim, C., Chuang, Y.Y., Kopf, J., Huang, J.B.: Robust dynamic radiance fields. In: Proceedings of the IEEE/CVF Conference on Computer Vision and Pattern Recognition. pp. 13–23 (2023) [2](#)
 21. Martin-Brualla, R., Radwan, N., Sajjadi, M.S., Barron, J.T., Dosovitskiy, A., Duckworth, D.: Nerf in the wild: Neural radiance fields for unconstrained photo collections. In: Proceedings of the IEEE/CVF Conference on Computer Vision and Pattern Recognition. pp. 7210–7219 (2021) [2](#), [3](#), [5](#)
 22. Mattheus, J., Grobler, H., Abu-Mahfouz, A.M.: A review of motion segmentation: Approaches and major challenges. In: 2020 2nd International multidisciplinary information technology and engineering conference (IMITEC). pp. 1–8. IEEE (2020) [2](#)
 23. Mildenhall, B., Srinivasan, P.P., Tancik, M., Barron, J.T., Ramamoorthi, R., Ng, R.: Nerf: Representing scenes as neural radiance fields for view synthesis. *Communications of the ACM* **65**(1), 99–106 (2021) [2](#), [5](#)
 24. Müller, T.: tiny-cuda-nn (2021), <https://github.com/NVlabs/tiny-cuda-nn> [8](#), [10](#)
 25. Müller, T., Evans, A., Schied, C., Keller, A.: Instant neural graphics primitives with a multiresolution hash encoding. *ACM Transactions on Graphics (ToG)* **41**(4), 1–15 (2022) [3](#), [5](#), [10](#)
 26. Neuhold, G., Ollmann, T., Rota Bulò, S., Kotschieder, P.: The mapillary vistas dataset for semantic understanding of street scenes. In: Proceedings of the IEEE international conference on computer vision. pp. 4990–4999 (2017) [11](#)
 27. Ost, J., Mannan, F., Thueray, N., Knodt, J., Heide, F.: Neural scene graphs for dynamic scenes. In: Proceedings of the IEEE/CVF Conference on Computer Vision and Pattern Recognition. pp. 2856–2865 (2021) [2](#), [4](#)
 28. Park, K., Sinha, U., Barron, J.T., Bouaziz, S., Goldman, D.B., Seitz, S.M., Martin-Brualla, R.: Nerfies: Deformable neural radiance fields. In: Proceedings of the IEEE/CVF International Conference on Computer Vision. pp. 5865–5874 (2021) [2](#), [3](#), [4](#)
 29. Park, K., Sinha, U., Hedman, P., Barron, J.T., Bouaziz, S., Goldman, D.B., Martin-Brualla, R., Seitz, S.M.: Hypernerf: A higher-dimensional representation for topologically varying neural radiance fields. arXiv preprint arXiv:2106.13228 (2021) [2](#), [3](#), [4](#)

30. Park, S., Son, M., Jang, S., Ahn, Y.C., Kim, J.Y., Kang, N.: Temporal interpolation is all you need for dynamic neural radiance fields. In: Proceedings of the IEEE/CVF Conference on Computer Vision and Pattern Recognition. pp. 4212–4221 (2023) [2](#), [3](#)
31. Paszke, A., Gross, S., Massa, F., Lerer, A., Bradbury, J., Chanan, G., Killeen, T., Lin, Z., Gimelshein, N., Antiga, L., et al.: Pytorch: An imperative style, high-performance deep learning library. *Advances in neural information processing systems* **32** (2019) [10](#)
32. Pumarola, A., Corona, E., Pons-Moll, G., Moreno-Noguer, F.: D-nerf: Neural radiance fields for dynamic scenes. In: Proceedings of the IEEE/CVF Conference on Computer Vision and Pattern Recognition. pp. 10318–10327 (2021) [4](#)
33. Rematas, K., Liu, A., Srinivasan, P.P., Barron, J.T., Tagliasacchi, A., Funkhouser, T., Ferrari, V.: Urban radiance fields. In: Proceedings of the IEEE/CVF Conference on Computer Vision and Pattern Recognition. pp. 12932–12942 (2022) [3](#), [8](#)
34. Sabour, S., Vora, S., Duckworth, D., Krasin, I., Fleet, D.J., Tagliasacchi, A.: Robustnerf: Ignoring distractors with robust losses. In: Proceedings of the IEEE/CVF Conference on Computer Vision and Pattern Recognition. pp. 20626–20636 (2023) [3](#), [6](#), [8](#), [11](#), [12](#), [21](#), [22](#), [23](#)
35. Saunders, K., Vogiatzis, G., Manso, L.J.: Dyna-dm: Dynamic object-aware self-supervised monocular depth maps. In: 2023 IEEE International Conference on Autonomous Robot Systems and Competitions (ICARSC). pp. 10–16. IEEE (2023) [4](#)
36. Schonberger, J.L., Frahm, J.M.: Structure-from-motion revisited. In: Proceedings of the IEEE conference on computer vision and pattern recognition. pp. 4104–4113 (2016) [2](#)
37. Schönberger, J.L., Zheng, E., Frahm, J.M., Pollefeys, M.: Pixelwise view selection for unstructured multi-view stereo. In: Computer Vision–ECCV 2016: 14th European Conference, Amsterdam, The Netherlands, October 11–14, 2016, Proceedings, Part III 14. pp. 501–518. Springer (2016) [2](#)
38. Sharma, P., Tewari, A., Du, Y., Zakharov, S., Ambrus, R.A., Gaidon, A., Freeman, W.T., Durand, F., Tenenbaum, J.B., Sitzmann, V.: Neural groundplans: Persistent neural scene representations from a single image. In: International Conference on Learning Representations (2023) [9](#), [20](#)
39. Siddiqui, Y., Porzi, L., Bulò, S.R., Müller, N., Nießner, M., Dai, A., Kotschieder, P.: Panoptic lifting for 3d scene understanding with neural fields. In: Proceedings of the IEEE/CVF Conference on Computer Vision and Pattern Recognition. pp. 9043–9052 (2023) [7](#)
40. Tonderski, A., Lindström, C., Hess, G., Ljungbergh, W., Svensson, L., Petersson, C.: Neurad: Neural rendering for autonomous driving. arXiv preprint arXiv:2311.15260 (2023) [2](#)
41. Tschernezki, V., Laina, I., Larlus, D., Vedaldi, A.: Neural feature fusion fields: 3d distillation of self-supervised 2d image representations. In: 2022 International Conference on 3D Vision (3DV). pp. 443–453. IEEE (2022) [3](#)
42. Tschernezki, V., Larlus, D., Vedaldi, A.: Neuraldiff: Segmenting 3d objects that move in egocentric videos. In: 2021 International Conference on 3D Vision (3DV). pp. 910–919. IEEE (2021) [4](#)
43. Turki, H., Zhang, J.Y., Ferroni, F., Ramanan, D.: Suds: Scalable urban dynamic scenes. In: Proceedings of the IEEE/CVF Conference on Computer Vision and Pattern Recognition. pp. 12375–12385 (2023) [4](#), [11](#), [12](#), [13](#), [22](#), [23](#)

44. Wang, F., Chen, Z., Wang, G., Song, Y., Liu, H.: Masked space-time hash encoding for efficient dynamic scene reconstruction. arXiv preprint arXiv:2310.17527 (2023) [2](#), [3](#)
45. Wang, F., Louys, A., Piasco, N., Bennehar, M., Roldão, L., Tsishkou, D.: Planerf: Svd unsupervised 3d plane regularization for nerf large-scale scene reconstruction. arXiv preprint arXiv:2305.16914 (2023) [9](#)
46. Wang, Z., Bovik, A.C., Sheikh, H.R., Simoncelli, E.P.: Image quality assessment: from error visibility to structural similarity. *IEEE transactions on image processing* **13**(4), 600–612 (2004) [8](#), [11](#)
47. Wu, T., Zhong, F., Tagliasacchi, A., Cole, F., Oztireli, C.: D²nerf: Self-supervised decoupling of dynamic and static objects from a monocular video. *Advances in Neural Information Processing Systems* **35**, 32653–32666 (2022) [2](#), [4](#), [5](#), [9](#), [11](#), [12](#), [13](#), [20](#), [22](#), [23](#)
48. Wu, Z., Liu, T., Luo, L., Zhong, Z., Chen, J., Xiao, H., Hou, C., Lou, H., Chen, Y., Yang, R., et al.: Mars: An instance-aware, modular and realistic simulator for autonomous driving. In: *CAAI International Conference on Artificial Intelligence*. pp. 3–15. Springer Nature Singapore Singapore (2023) [2](#)
49. Xiao, P., Shao, Z., Hao, S., Zhang, Z., Chai, X., Jiao, J., Li, Z., Wu, J., Sun, K., Jiang, K., et al.: Pandaset: Advanced sensor suite dataset for autonomous driving. In: *2021 IEEE International Intelligent Transportation Systems Conference (ITSC)*. pp. 3095–3101. IEEE (2021) [11](#)
50. Xu, Y., Chai, M., Shi, Z., Peng, S., Skorokhodov, I., Siarohin, A., Yang, C., Shen, Y., Lee, H.Y., Zhou, B., et al.: Discoscene: Spatially disentangled generative radiance fields for controllable 3d-aware scene synthesis. In: *Proceedings of the IEEE/CVF Conference on Computer Vision and Pattern Recognition*. pp. 4402–4412 (2023) [2](#), [4](#)
51. Yan, Y., Lin, H., Zhou, C., Wang, W., Sun, H., Zhan, K., Lang, X., Zhou, X., Peng, S.: Street gaussians for modeling dynamic urban scenes. arXiv preprint arXiv:2401.01339 (2024) [2](#)
52. Yang, J., Ivanovic, B., Litany, O., Weng, X., Kim, S.W., Li, B., Che, T., Xu, D., Fidler, S., Pavone, M., et al.: Emernerf: Emergent spatial-temporal scene decomposition via self-supervision. arXiv preprint arXiv:2311.02077 (2023) [4](#), [11](#), [12](#), [13](#), [22](#), [23](#)
53. Yang, Y., Yang, Y., Guo, H., Xiong, R., Wang, Y., Liao, Y.: Urbangiraffe: Representing urban scenes as compositional generative neural feature fields. arXiv preprint arXiv:2303.14167 (2023) [2](#)
54. Yang, Z., Chen, Y., Wang, J., Manivasagam, S., Ma, W.C., Yang, A.J., Urtasun, R.: Unisim: A neural closed-loop sensor simulator. In: *Proceedings of the IEEE/CVF Conference on Computer Vision and Pattern Recognition*. pp. 1389–1399 (2023) [2](#)
55. Ye, W., Yu, X., Lan, X., Ming, Y., Li, J., Bao, H., Cui, Z., Zhang, G.: Deflowslam: Self-supervised scene motion decomposition for dynamic dense slam. arXiv preprint arXiv:2207.08794 (2022) [4](#)
56. Yuan, W., Lv, Z., Schmidt, T., Lovegrove, S.: Star: Self-supervised tracking and reconstruction of rigid objects in motion with neural rendering. In: *Proceedings of the IEEE/CVF Conference on Computer Vision and Pattern Recognition*. pp. 13144–13152 (2021) [4](#), [9](#), [20](#)
57. Zhang, R., Isola, P., Efros, A.A., Shechtman, E., Wang, O.: The unreasonable effectiveness of deep features as a perceptual metric. In: *Proceedings of the IEEE conference on computer vision and pattern recognition*. pp. 586–595 (2018) [11](#)

58. Zhang, X., Kundu, A., Funkhouser, T., Guibas, L., Su, H., Genova, K.: Nerflets: Local radiance fields for efficient structure-aware 3d scene representation from 2d supervision. In: Proceedings of the IEEE/CVF Conference on Computer Vision and Pattern Recognition. pp. 8274–8284 (2023) [3](#)
59. Zhi, S., Laidlow, T., Leutenegger, S., Davison, A.J.: In-place scene labelling and understanding with implicit scene representation. In: Proceedings of the IEEE/CVF International Conference on Computer Vision. pp. 15838–15847 (2021) [6](#), [8](#)
60. Zhou, X., Lin, Z., Shan, X., Wang, Y., Sun, D., Yang, M.H.: Drivinggaussian: Composite gaussian splatting for surrounding dynamic autonomous driving scenes. arXiv preprint arXiv:2312.07920 (2023) [2](#)

A Implementation Details

A.1 Data Processing

In our experiments, we downsample Pandaset images by a factor of 4 (480×270) and KITTI-360 by a factor of 2 (704×188). The selected scenes from KITTI-360 are summarized in Tab. [3](#). For Pandaset, we used sequences 023, 042, and 043. We specifically selected those scenes because they feature multiple dynamic objects while providing sufficient views of the background regions.

Table 3: Selected KITTI-360 sequences for training, with skip step of 2.

Sequence	Scene	Start Frame	End Frame	#Frames per camera
0	0002	4970	5230	130
1	0003	100	330	115
2	0007	2680	2930	125
3	0010	910	1160	125

For semantic awareness, the classes we assume to be dynamic and keep the contribution in the dynamic semantic head are: “Person”, “Rider”, “Car”, “Truck”, “Bus”, “Train”, “Motorcycle”, “Bicycle”, “Bicyclist”, “Motorcyclist”, and “Unknown vehicle”.

A.2 Architecture

We adopt a proposal-based coarse-to-fine sampling technique [\[2\]](#) using two proposal models with the number of samples being [\[128, 96\]](#) for the proposal models, and 48 for the final model. Our hash grids have the size of 2^{19} for 16 levels with the base resolution and finest resolution of 16 and 2048 respectively. Additionally, our dynamic hash grid allows 4D inputs, which means that the intermediate feature vector is computed through a quadrilinear interpolation of 16 grid point vectors instead of the 8 used for the 3D hash grid. The static branch of our model is equipped with a 16-dimension per-frame embedding to adapt to varying lighting conditions.

A.3 Losses

The individual components used in the dynamic regularization loss are:

Static-dynamic entropy factorization loss. We assume that any point in space can either belong to a static or dynamic object at one time, but not both, and encourage the transparency ratio at each point to be either 0 or 1, aiding the model in achieving a less entangled decomposition:

$$\mathcal{L}_{\mathcal{H}} = \mathbb{E} \left[\mathcal{H} \left(\frac{\alpha^D}{\alpha^S + \alpha^D} \right) (\alpha^S + \alpha^D) \right], \quad (10)$$

where $\mathcal{H}(x) = -(x \cdot \log(x) + (1-x) \cdot \log(1-x))$ is the binary entropy function and the term is weighted by the total transparency $(\alpha^S + \alpha^D)$ so that a point is allowed to have an empty density, as done in [56].

Dynamic sparsity losses. The sparsity terms take as input densities σ^D and shadow ρ decoded from the dynamic field respectively and encourage those values to be sparse [38, 47]:

$$\mathcal{L}_{\sigma^D} = \mathbb{E} \left[\frac{1}{K} \sum_{i=1}^K \sigma_i^D \right]_{\mathbf{r} \in \mathcal{R}} \quad \text{and} \quad \mathcal{L}_{\rho} = \mathbb{E} \left[\frac{1}{K} \sum_{i=1}^K T_i \alpha_i \rho_i^2 \right]_{\mathbf{r} \in \mathcal{R}}. \quad (11)$$

A.4 Training

We trained RoDUS for 50 epochs using the Adam optimizer with a batch size of 200. The learning rate was set to 0.01, and we used cosine decay to decrease it to 0.0001. The rays are grouped in 15×15 patches to suit DSSIM, planar regularization, and robust losses. Table 4 summarizes the hyperparameters used for the training of RoDUS, we do not require manual tuning for each scene, but we believe that such tuning could potentially further enhance performance.

Table 4: Training hyperparameters

Parameter	Value
λ_d	0.5
λ_{sem}	0.1
λ_{sky}	0.03
λ_{road}	0.1
λ_{σ^D}	0.05
λ_{ρ}	0.3
$\lambda_{\mathcal{H}}$	0.01

Baseline Implementations. We adapt the code in the official repository of each method: RobustNeRF¹, D²NeRF², SUDS³, EmerNeRF⁴ and modify their dataloaders. We search for the best robust loss threshold \mathcal{T}_{ϵ} for RobustNeRF, while the rest are trained with the default parameters provided in the repositories.

¹ <https://robustnerf.github.io/>

² <https://github.com/ChikaYan/d2nerf>

³ <https://github.com/hturki/suds>

⁴ <https://github.com/NVlabs/EmerNeRF>

B Additional Results

Fig. 10 and Fig. 11 show additional qualitative comparisons between our RoDUS and previous methods in static-dynamic decomposition and scene reconstruction. Fig. 12 displays RoDUS’s performance on other different scenes, demonstrating that RoDUS’s dynamic branch is able to classify moving objects from parked vehicles or other static instances. Furthermore, RoDUS can be trained from noisy semantic annotations, leading to a scene-consistent semantic representation. A combination of multiple modalities also supports the model in reconstructing and segmenting thin structures and objects (*e.g.* light poles, and traffic signs).

C Additional Ablation and Analysis

C.1 Robust Kernel Threshold

We explain the choice of percentile threshold \mathcal{T}_ϵ used in RobustNeRF [34] and report qualitative results in Fig. 13. With $\mathcal{T}_\epsilon = 0.7$, there are still a lot of structures that could not be learned (*e.g.* the far away building), when we increase \mathcal{T}_ϵ to 0.9, the shadow regions started to appear. As a result, we choose $\mathcal{T}_\epsilon = 0.75$ as it yields the best visual quality with the least artifacts. Correspondingly, the kernel saturates as we observed no improvement as the training continues. Notice that the model could not learn the road marking in any case.

C.2 Shadow Handling

Shadows cast by dynamic objects are also time-varying and modeled separately in our model. Fig. 14 shows that RoDUS successfully decouples the shadows from the scene.

D Discussions

D.1 Ethical Concern

Our method mainly serves the purpose of removing dynamic vehicles from the scenes. While such methods hold promise in augmenting training environments for autonomous vehicles by simulating diverse scenarios, considering the act of modifying real-world driving data for inappropriate motives (*e.g.* erasing actors, generating fake content) is **not** encouraged. Altering records for any purpose carries the risk of distorting the true nature of driving events and the credibility of data-driven insights. In contrast, we would be delighted to see directions that focus on detecting image forgery for such methods. We believe this area of study could hold significant potential for advancements in the field, providing opportunities to enhance the robustness and security of digital content.

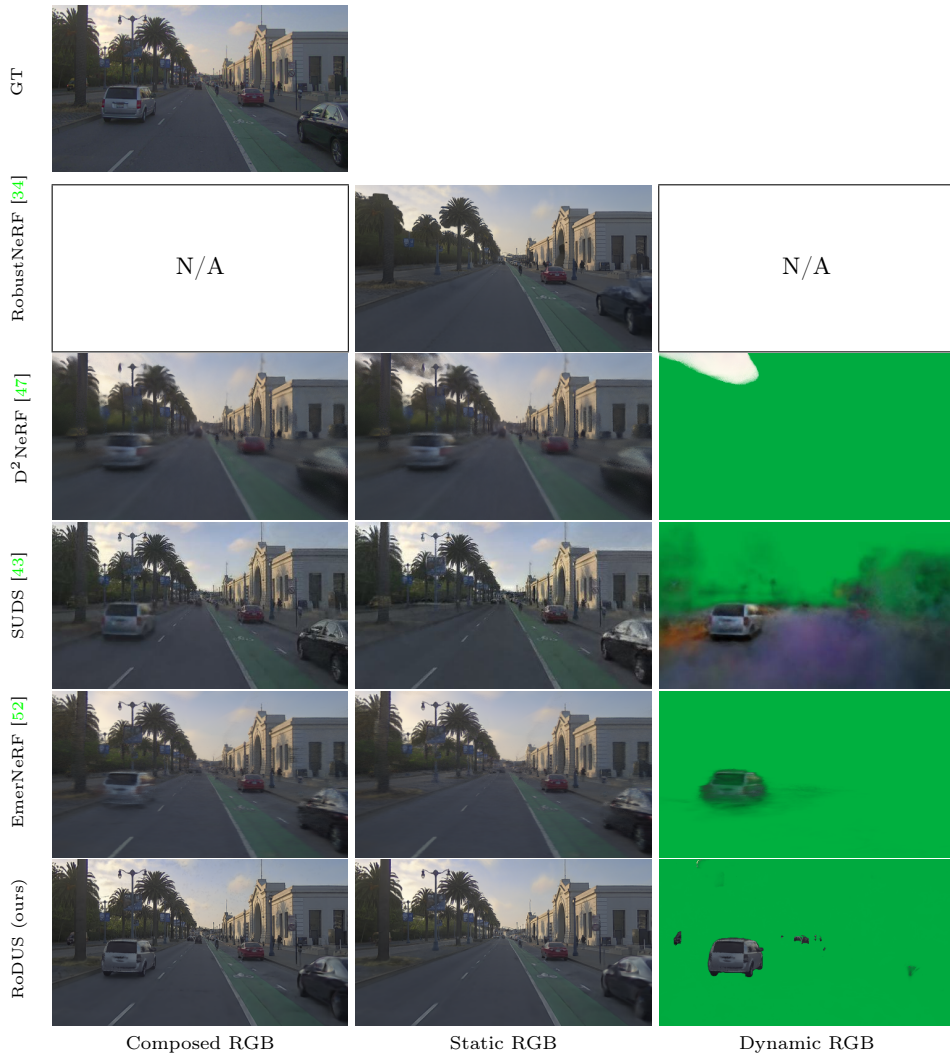


Fig. 10: Additional qualitative comparisons on Pandaset.

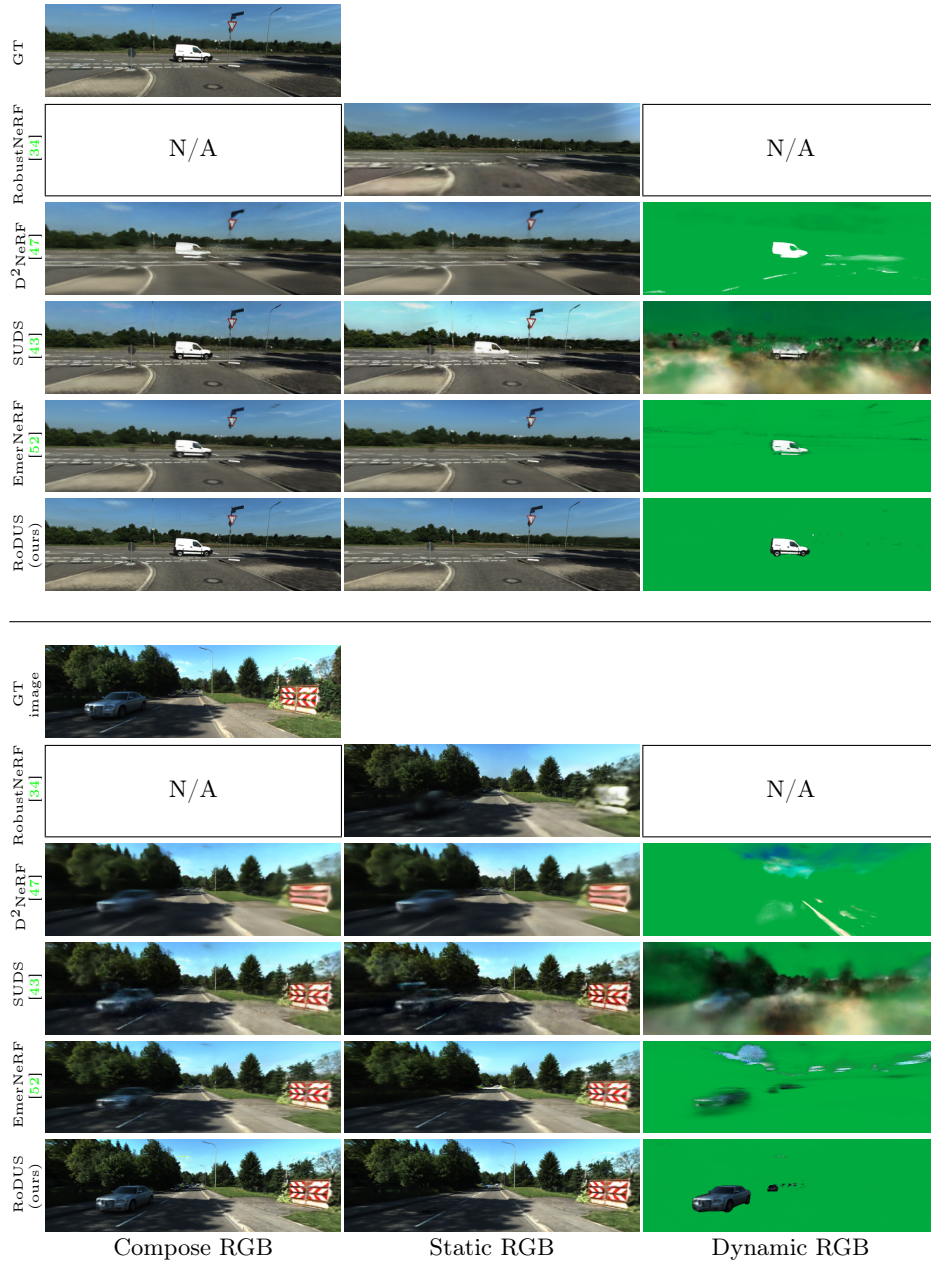


Fig. 11: Additional qualitative comparisons on KITTI-360.

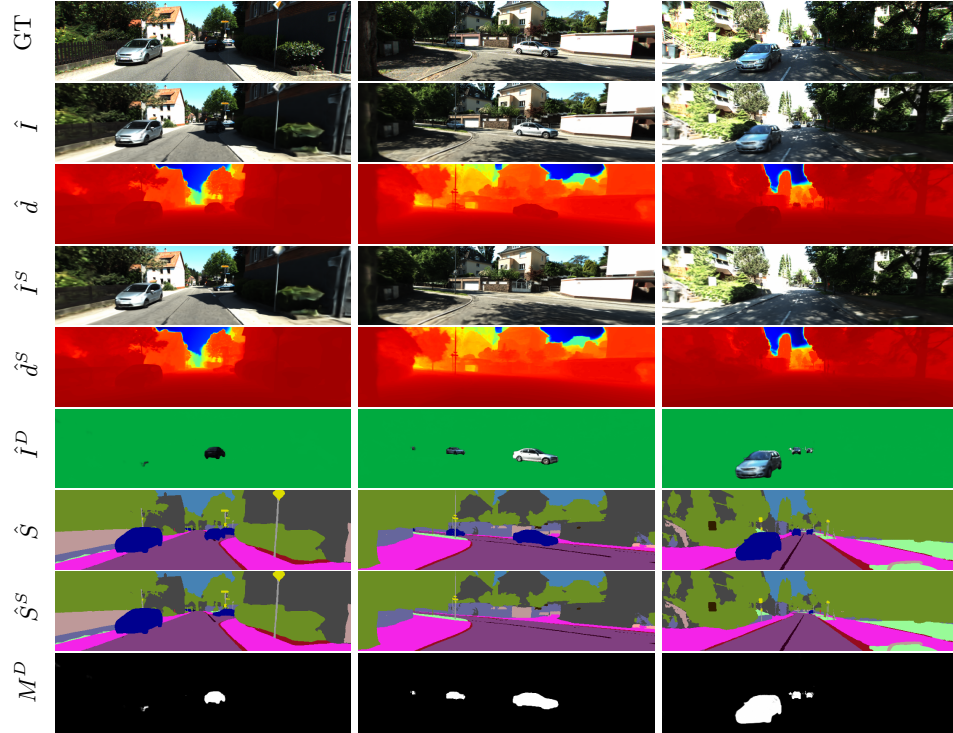


Fig. 12: Additional results on RoDUS’s capability.

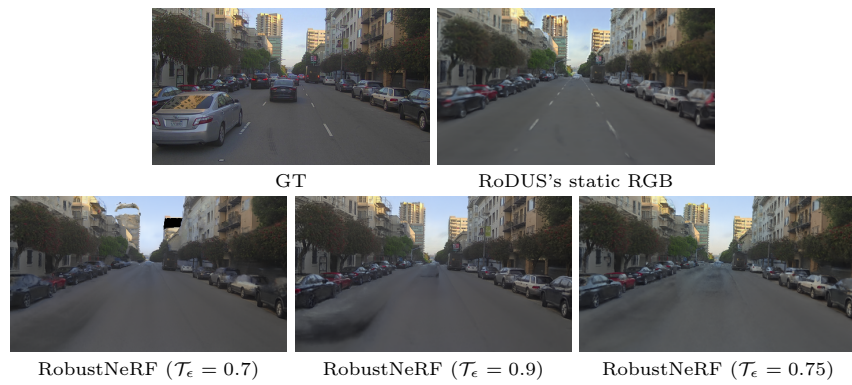


Fig. 13: Qualitative comparison on static RGB image with different threshold values.



Fig. 14: We obtain the shadow mask by applying volumetric rendering on the shadow ratio ρ , demonstrating that the model is learning the correct shadow regions.

D.2 Limitation

Apart from the main limitation mentioned in the paper, we also encountered several problems that are related to most NeRF-based methods in general: RoDUS demands precise camera poses, which require multiple sources of odometry when working with outdoor, high-dynamic scenes. Furthermore, for RoDUS to yield good reconstruction, it relies on a substantial number of input images from multiple views, making it less effective in few-shot settings.